Computer Methods in Applied Mechanics and Engineering 449 (2026) 118495

Contents lists available at ScienceDirect

Comput. Methods Appl. Mech. Engrg.

journal homepage: www.elsevier.com/locate/cma

Explicit high-order time and space accurate isogeometric collocation method for the dynamics of geometrically exact beams

Giulio Ferri, Enzo Marino *

Department of Civil and Environmental Engineering, University of Florence, Via di S. Marta 3, 50139, Firenze, Italy

ARTICLE INFO

Keywords:
Isogeometric analysis
Isogeometric collocation
Explicit dynamics
Geometrically exact beams
Runge-Kutta-Munthe-Kaas

ABSTRACT

The efficient simulation of highly deformable mechanical systems under fast and complex dynamic loads necessitates the advancement of explicit computational methods. Traditional explicit schemes, which leverage diagonal mass matrices and mass-scaling techniques, have improved efficiency. However, for problems evolving on nonlinear manifolds, such as $\mathbb{R}^3 \times SO(3)$, their accuracy remains limited to second-order in time. This limitation becomes even more critical when combined with high-order spatial techniques, such as Isogeometric Collocation (IGA-C), since it prevents the full exploitation of the spatial discretization potentialities. To address this gap, we propose a novel, fully explicit, high-order method for the dynamics of geometrically exact beams. The approach extends the Runge-Kutta-Munthe-Kaas (RKMK) scheme, originally developed for rigid body systems, to nonlinear partial differential equations governing deformable structures. The strong form of the problem is efficiently discretized in space using IGA-C, eliminating the need for element integration. Through various numerical tests, we demonstrate the ability of the proposed formulation to achieve high-order accuracy in time and space. Although the paper is focused on geometrically exact beams, the method is general and lays the ground for a promising extension to geometrically exact shells.

1. Introduction

The need for increasingly efficient and accurate computational tools for the analysis of highly deformable mechanical systems under fast and complex dynamic loads requires the enhancement of existing explicit methods. In explicit dynamics, efficiency is sought through discretization schemes that bypass time-consuming operations of matrix inversion by means of diagonal mass matrices. These approaches have been adopted in finite element-based methods [1,2], but they are also being investigated for those discretization schemes that adopt non-interpolatory basis functions, such as NURBS [3] and B-Splines [4–7]. Also mass-scaling techniques, which allow increasing the critical time step, are extremely appealing in explicit dynamics [8]. These methods have been studied for both finite elements [9] and NURBS discretizations [10]. Recently, they have been specifically developed for shear-deformable structural elements in [11,12], where a selective mass-scaling of the transverse shear frequencies permits targeting high accuracy, preserving both linear and angular momenta.

Higher efficiency and accuracy are also pursued through high-order schemes. Runge-Kutta (RK) methods [13,14] are among the most widely employed high-order time-discretization schemes for the solution of Partial Differential Equations (PDEs) governing the dynamics of solids and structures. However, in most of the cases, RK schemes have been successfully developed for the solution

* Corresponding author.
E-mail address: enzo.marino@unifi.it (E. Marino).

https://doi.org/10.1016/j.cma.2025.118495
Received 21 July 2025; Received in revised form 9 September 2025; Accepted 9 October 2025
Available online 10 November 2025
0045-7825/© 2025 The Author(s). Published by Elsevier B.V. This is an open access article under the CC BY-NC-ND license (http://creativecommons.org/licenses/by-nc-nd/4.0/).

of problems evolving on linear spaces, i.e., $\mathbb{R}^3$. When rotational dynamic problems are concerned, such as for geometrically exact beams [15–18] and shells [11,12,19,20], standard RK methods are not directly applicable since they violate the underlying geometric structure of the configuration manifold that is based on the rotations (Lie) group SO(3) [21]. An extension of the standard RK scheme, suitable for problems evolving on nonlinear manifolds and referred to as Runge-Kutta-Munthe-Kaas (RKMK), was proposed in [22,23]. Originally, RKMK methods were employed for rigid and multi-body dynamics, such as articulated robots, quad-rotors and load transportation problems [24–26]. In spite of the large potential of the RKMK methods, to the best of the Authors' knowledge, it appears that they have not yet been employed in the study of the dynamics of deformable continua.

Since the late 1980s, beginning with the seminal works of Simo & Vu-Quoc [17] and Cardona & Geradin [27], numerous formulations, primarily based on standard finite element analysis (FEA), have been proposed to model the dynamics of geometrically exact spatial beams. Advantages and limitations of various time integration schemes have been explored in several studies, see for example [28–43]. See also [44,45] for a review. An explicit version [46] of the Newmark algorithm for SO(3) was extended to geometrically exact beams in [47] and further developed in [48] using a geometrically consistent predictor multi-corrector scheme. Although the above works significantly contributed to the advancement of time integration schemes for the rotational dynamics of structures, they all have the time-accuracy limited to the second-order. This limitation becomes especially critical when these time integration schemes are combined with high-order space discretization technologies, as in the case of Isogeometric Analysis (IGA) [49–51]. Within the IGA framework, the Isogeometric Collocation (IGA-C) method [52–54] is particularly attractive for explicit dynamics thanks to its efficiency [55–57]. The method discretizes the strong form of the governing equations using one evaluation (collocation) point per degree of freedom. As opposed to standard Galerkin methods, IGA-C bypasses element integration while preserving the IGA attributes in terms oh high-order accuracy and geometric capabilities. In addition to explicit ([47,48]) and implicit ([58,59]) dynamics of geometrically exact beams, IGA-C has been successfully employed for a wide range of problems, including geometrically exact beams in statics with elastic materials [60,61], inelastic [62] and rate-dependent materials [63], as well as contact [64,65], phase-field [66,67] and electromechanics [68]. Explicit predictor-multicorrector algorithms for IGA-C were proposed in [55,56]. In [56] it was demonstrated the possibility to achieve higher-order time accuracy for linear elastodynamic problems through standard Runge-Kutta methods.

With the present work we intend to fill the gap by proposing a high-order time and space-accurate method for the explicit dynamics of geometrically exact beams. The RKMK scheme is extended to solve the nonlinear governing equations evolving on the beam configuration manifold, $\mathbb{R}^3 \times SO(3)$, whose spatial discretization is made through the IGA-C method. Importantly, an efficient treatment of the Neumann boundary conditions [64] allows to obtain a formulation that does not require any matrix inversion or any decoupling treatment as done in [48]. Moreover, with the proposed formulation, lumping procedures [5,6] or iterative schemes, such as the predictor multi-corrector approach [48,56], are not necessary. Furthermore, we remark that the developed framework is completely general and can be employed for any rotational dynamic problems, beyond geometrically exact beams. In particular we foresee a promising extension to geometrically exact shells.

The paper is structured as follows. In Section 2, the RKMK method for geometrically exact beams is presented, introducing first the standard RK method, and then its SO(3)-consistent version suitable for differential problems evolving on the beam configuration manifold. In Section 3, we briefly recall the explicit version of the dynamic governing equations for geometrically-exact Timoshenko beams, written in the spatial setting. We also present the time and space discretization of the problem, with particular attention on recasting the RKMK scheme on the beam configuration manifold and on the SO(3)-consistent geometry update. In Section 4, we assess the performance of the method through challenging numerical tests. Finally, the main conclusions of the work are drawn in Section 5.

2. The RKMK method for geometrically exact beams

In this section, we present the formulation of the RKMK method for the geometrically exact beam problem. For convenience, at first we briefly review the classical RK time-integrator scheme. Then, we recall the kinematics of geometrically exact, shear-deformable beams with a focus on the underlying geometric structure. Finally, the RKMK is introduced and applied to the beam problem.

2.1. The RK method for PDEs evolving on linear spaces

Explicit RK methods allow to approximate the solution of differential equation given in the following form

$$\dot{y}(t) = f(t, y(t)), \qquad y(0) = y_0 \,, \tag{1}$$

where $y(t)$ is a function of time t and $(\dot{\circ})$ indicates the time derivative. Denoting the current time instant $t^n = h(n-1)$, $h > 0$ being the step size, the value $y^{n+1} := y(t^{n+1})$ is

$$y^{n+1} = y^n + h \sum_{r=1}^{N} b_r k_r \,, \tag{2}$$

where

$$k_r = f(t_r^n, y_r^n), \quad \text{with} \quad t_r^n = t^n + c_r h \quad \text{and} \quad y_r^n = y^n + h \sum_{l=1}^{N} d_{rl} k_l \,. \tag{3}$$

In the above equations, N denotes the number of RK stages required to compute y^{n+1}. N is directly related to the order, i.e., the time-accuracy, of the method; d_{lr} is the RK matrix, whereas b_r and c_r are referred to as weights and nodes, respectively. Different RK methods are associated with different values of these coefficients, which are often arranged in the so-called Butcher tableau [13,69]

$$\begin{array}{c|c} \boldsymbol{c} & \boldsymbol{D} \\ \hline & \boldsymbol{b}^{\mathsf{T}} \end{array} \tag{4}$$

where $\boldsymbol{c}^{\mathsf{T}} = [c_1, c_2, \dots, c_N]^{\mathsf{T}}$, $\boldsymbol{b}^{\mathsf{T}} = [b_1, b_2, \dots, b_N]^{\mathsf{T}}$, and $\boldsymbol{D} = [d_{rl}]$, $l, r = 1, 2, \dots, N$. Note that the methods are explicit when, as in our case, $d_{rl} = 0$ for $r \le l$. For convenience, in Appendix A, we report the values of these coefficients with accuracy up to the sixth-order.

2.2. The fundamental kinematic assumption for shear-deformable beams

The standard RK scheme recalled in Section 2.1. is valid only if the differential problem evolves on a linear space, e.g. if $y(t)$ and $f(t, y(t))$ belong to $\mathbb{R}$ or $\mathbb{R}^3$.

To clarify why the standard RK method cannot be directly applied to the problem of geometrically exact beams, we need to recall the fundamental kinematic assumptions underlying the problem [70,71].

Let $\mathcal{B}$ be a beam-shaped material body. The shear-deformable geometrically exact theory assumes that the motion $\boldsymbol{\varphi}(t, \boldsymbol{p})$ of any material point, $\boldsymbol{p} \in \mathcal{B}$, is completely determined by the motion of the beam centroid, $\boldsymbol{c}(t, \boldsymbol{q}) \in \mathbb{R}^3$, and the rigid rotation of the beam cross-section, $\mathbf{R}(t, \boldsymbol{q}) \in \mathrm{SO}(3)$, as follows

$$\boldsymbol{\varphi}(t, \boldsymbol{p}) = \boldsymbol{c}(t, \boldsymbol{q}) + \mathbf{R}(t, \boldsymbol{q})(\boldsymbol{p} - \boldsymbol{q}) \quad \text{for each} \quad t \in \boldsymbol{T}\,, \boldsymbol{p} \in \mathcal{B}\,, \tag{5}$$

where $\boldsymbol{q} \in \mathcal{S} \subset \mathcal{B}$ denotes the position of the beam centroid. $\mathcal{S}$ is the beam axis made of all cross sections' centroids. On $\mathcal{S}$ we define a one-dimensional coordinate system $s : \mathcal{S} \to [0, L] \subset \mathbb{R}$ such that $\boldsymbol{q} \mapsto s(\boldsymbol{q}) \in [0, L]$. For the sake of brevity, in the following we will use only s, instead of $s(\boldsymbol{q})$. Under the kinematic assumption in Eq. (5), any cross-section is a two-dimensional rigid body hinged to the beam centroid. Therefore, at any time instant $t \in \boldsymbol{T}$, the beam configuration is completely described by $\boldsymbol{c}$ and $\mathbf{R}$ that define the configuration manifold $\mathcal{C}$

$$\mathcal{C} = \left\{(\boldsymbol{c}, \mathbf{R}) \,|\, \boldsymbol{c} : \boldsymbol{T} \times \mathcal{S} \to \mathbb{R}^3 \,, \mathbf{R} : \boldsymbol{T} \times \mathcal{S} \to \mathrm{SO}(3)\right\}. \tag{6}$$

The concept of local linear approximation of the configuration manifold is crucial to properly build the time integrator. First we recall that the tangent space to the configuration manifold at $(\boldsymbol{c}, \mathbf{R}) \in \mathcal{C}$ is $T_{(\boldsymbol{c},\mathbf{R})}\mathcal{C} = T_{\boldsymbol{c}}\mathbb{R}^3 \times T_{\mathbf{R}}\mathrm{SO}(3)$. As recalled in [60], let $\varepsilon \mapsto \boldsymbol{\gamma}(\varepsilon) = (\boldsymbol{c}_\varepsilon, \mathbf{R}_\varepsilon) \in \mathcal{C}$ be a curve on $\mathcal{C}$ with $\boldsymbol{\gamma}(0) = (c, \mathbf{R})$ and such that $(\boldsymbol{c}_\varepsilon, \mathbf{R}_\varepsilon) = (\boldsymbol{c} + \varepsilon\boldsymbol{\eta}, \exp(\varepsilon\widetilde{\boldsymbol{\vartheta}})\mathbf{R})$.

By definition of tangent space [21], $d\gamma(\varepsilon)/d\varepsilon|_{\varepsilon=0} = (\boldsymbol{\eta}, \widetilde{\boldsymbol{\vartheta}}\mathbf{R})$ represents a tangent vector to $\mathcal{C}$ at $(\boldsymbol{c}, \mathbf{R})$. We recognize that the tangent space to the manifold $\mathbb{R}^3$ (the affine environmental space) at $\boldsymbol{c}$ is again the standard vector space $\mathbb{R}^3$ applied in $\boldsymbol{c}$. Whereas, the (spatial) tangent space to the SO(3) at $\mathbf{R}$ is defined as $T_{\mathbf{R}}\mathrm{SO}(3) := \left\{\tilde{\boldsymbol{\vartheta}}\mathbf{R} \,|\, \tilde{\boldsymbol{\vartheta}} \in \mathrm{so}(3)\,, \mathbf{R} \in \mathrm{SO}(3)\right\}$ [17,34]. Note that $\boldsymbol{\eta}(t, s) \in T_{\boldsymbol{c}}\mathbb{R}^3 \equiv \mathbb{R}^3$ represents an incremental displacement field superimposed to the current (spatial) configuration of the centroid line $\boldsymbol{c}(t, s)$; whereas $\widetilde{\boldsymbol{\vartheta}}(t, s)$, such that $\widetilde{\boldsymbol{\vartheta}}\mathbf{R} \in T_{\mathbf{R}}\mathrm{SO}(3)$, represents an incremental rotation field superimposed to the current (spatial) rotation field $\mathbf{R}(t, s)$.

2.3. RK methods for PDEs evolving on the beam configuration manifold

For problems evolving on manifolds, such as $\mathcal{C}$, the RK must be formulated on the tangent space to manifold (see Section 2.2). More precisely, for the translational part $\boldsymbol{c}(t, s)$, since the tangent space is basically $\mathbb{R}^3$, the RK method can be used in its standard form. In this case the differential equation takes the form

$$\dot{\boldsymbol{c}}(t, s) = \boldsymbol{v}(t, s) \quad \text{with} \quad \boldsymbol{c}(0, s) = \boldsymbol{c}_0(s) \in \mathbb{R}^3\,, \tag{7}$$

which can be straightforwardly rewritten in the form

$$\dot{\boldsymbol{\eta}}(t, s) = \boldsymbol{v}(t, s) \quad \text{with} \quad \boldsymbol{\eta}(0, s) = \mathbf{0} \in \mathbb{R}^3\,. \tag{8}$$

In the above equations, $\boldsymbol{v}(t, s)$ and $\boldsymbol{\eta}(t, s)$ are the spatial translational velocity and displacement of centroid, respectively, while $\boldsymbol{c}_0(s)$ denotes the initial position of the beam centroid. At time t^{n+1}, following Eq. (2), the time-discretized version of Eqs. (7) becomes

$$\boldsymbol{c}^{n+1} = \boldsymbol{c}^n + \boldsymbol{\eta}^n\,, \tag{9}$$

where we have set

$$\boldsymbol{\eta}^n = h \sum_{r=1}^{N} b_r \boldsymbol{k}_{\eta_r}\,. \tag{10}$$

In contrast, if $y(t)$ belongs to the Lie group SO(3), as in the case of $\mathbf{R}(t, s)$, the classical RK methods must be reformulated in a geometrically consistent way since standard operations, such as additions are not defined. As mentioned above, we refer to the manifold-consistent RK method as RKMK method. The basic idea is to solve the differential equation locally approximating the group SO(3) with its Lie algebra (the tangent space at the identity of the group), so (3), representing the (local) linear space where standard operations can be carried out.

The rotational counterpart of Eq. (7) takes the form

$$\dot{\mathbf{R}}(t, s) = \widetilde{\boldsymbol{\omega}}(t, \mathbf{R}(t, s))\mathbf{R}(t, s), \qquad \mathbf{R}(0, s) = \mathbf{R}_0(s) \in \mathrm{SO}(3)\,, \tag{11}$$

where $\widetilde{\omega}(t, \mathbf{R}(t, s)) \in \mathrm{so}(3)$ is the spatial angular velocity (skew-symmetric tensor) whose associated vector is $\boldsymbol{\omega}(t, \mathbf{R}) = \mathrm{axial}(\widetilde{\boldsymbol{\omega}}(t, \mathbf{R}))$[1], and $\mathbf{R}_0(s)$ is the rotation operator of the beam initial configuration. Given a spatial rotation $t \mapsto \widetilde{\boldsymbol{\vartheta}}(t, s) \in \mathrm{so}(3)$ at $\mathbf{R}_0(s)$, the relationship between $\mathbf{R}_0(s)$ and its spatial incremental quantity is not immediate as in the case of $\boldsymbol{c}$ (Eqs. (7) and (8)). It can be demonstrated, see Appendix B, that the rotational problem Eq. (11) can be reformulated as

$$\dot{\boldsymbol{\vartheta}}(t, s) = d\exp^{-1}_{\widetilde{\boldsymbol{\vartheta}}} (\boldsymbol{\omega}(t, \mathbf{R}(t, s))), \qquad \boldsymbol{\vartheta}(0, s) = \mathbf{0}\,. \tag{12}$$

It is a noteworthy fact that $d\exp^{-1}_{\widetilde{\boldsymbol{\vartheta}}}$, as well as $d\exp_{\widetilde{\boldsymbol{\vartheta}}}$, are known in a closed form, see Appendix B.

We have now the fundamental tool to reinterpret the standard RK method (Eqs. (2)-(3)) in the context of SO(3). To compute $\mathbf{R}^{n+1}$, Eq. (2) takes the form

$$\mathbf{R}^{n+1} = \exp(\widetilde{\boldsymbol{\vartheta}}^{n})\mathbf{R}^{n}\,, \tag{13}$$

where we have set

$$\boldsymbol{\vartheta}^{n} = h \sum_{r=1}^{N} b_r \boldsymbol{k}_{\vartheta_r}\,, \tag{14}$$

in which, using Eq. (12),

$$\boldsymbol{k}_{\vartheta_r} = d\exp^{-1}_{\widetilde{\boldsymbol{\vartheta}}^{n}_{r}}(\widetilde{\boldsymbol{\omega}}^{n}_{r})\,. \tag{15}$$

In conclusion, the incremental versions Eqs. (8) and (12) of the problems in Eqs. (7) and (11) represent the crucial background to build, in the following sections, the complete differential problem governing the dynamics of geometrically exact beams to be solved with the RKMK method.

3. Explicit dynamics of geometrically exact beams

3.1. Balance equations

The governing equations for the geometrically exact beam problem in the spatial form are

$$\mu\dot{\boldsymbol{v}} = \mathbf{R}\widetilde{\boldsymbol{K}}\mathbb{C}_N\boldsymbol{\Gamma}_N + \mathbf{R}\mathbb{C}_N\boldsymbol{\Gamma}_{N,s} + \bar{\boldsymbol{n}}, \tag{16}$$

$$\boldsymbol{j}\dot{\boldsymbol{\omega}} + \widetilde{\boldsymbol{\omega}}\boldsymbol{j}\boldsymbol{\omega} = \mathbf{R}\widetilde{\boldsymbol{K}}\mathbb{C}_M\boldsymbol{K}_M + \mathbf{R}\mathbb{C}_M\boldsymbol{K}_{M,s} + \boldsymbol{c}_{,s} \times \mathbf{R}\mathbb{C}_N\boldsymbol{\Gamma}_N + \bar{\boldsymbol{m}}, \tag{17}$$

valid for $s \in (0, L)$ and $t \in (0, T]$. In the above equations, $(\circ)_{,s}$ denotes the derivative with respect to the coordinate s; μ is the mass per unit length of the beam; $\widetilde{\boldsymbol{K}} = \mathbf{R}^{\mathsf{T}}\mathbf{R}_{,s}$ is the material curvature tensor, whereas $\boldsymbol{\Gamma}_N = \mathbf{R}^{\mathsf{T}}\boldsymbol{c}_{,s} - \mathbf{R}_0^{\mathsf{T}}\boldsymbol{c}_{0,s}$ and $\boldsymbol{K}_M = \boldsymbol{K} - \boldsymbol{K}_0$ are the beam material strain measures. $\boldsymbol{j} = \mathbf{R}\boldsymbol{J}\mathbf{R}^{\mathsf{T}}$ is the (time-dependent) spatial inertia tensor, while $\boldsymbol{J}$ is its (time-independent) material counterpart. $\dot{\boldsymbol{\omega}} = \boldsymbol{\alpha}$ and $\boldsymbol{\omega}$ are the spatial angular acceleration and velocity vector, respectively. $\mathbb{C}_N$ and $\mathbb{C}_M$ are the elasticity tensors (see e.g., [15]), while $\bar{\boldsymbol{n}}$ and $\bar{\boldsymbol{m}}$ are the distributed external force and couples per unit length.

To complete the set of equations, initial conditions and boundary conditions are enforced as follows

$$\boldsymbol{v} = \boldsymbol{v}_0 \quad \text{with} \quad s \in (0, L) \quad \text{and} \quad t = 0\,, \tag{18}$$

$$\boldsymbol{\omega} = \boldsymbol{\omega}_0 \quad \text{with} \quad s \in (0, L) \quad \text{and} \quad t = 0\,. \tag{19}$$

$$\boldsymbol{\eta} = \bar{\boldsymbol{\eta}}_c \quad \text{or} \quad \boldsymbol{n} = \bar{\boldsymbol{n}}_c \quad \text{with} \quad s = \{0, L\}\,, t \in [0, T]\,, \tag{20}$$

$$\boldsymbol{\vartheta} = \bar{\boldsymbol{\vartheta}}_c \quad \text{or} \quad \boldsymbol{m} = \bar{\boldsymbol{m}}_c \quad \text{with} \quad s = \{0, L\}\,, t \in [0, T]\,, \tag{21}$$

where $\boldsymbol{v}_0$ and $\boldsymbol{\omega}_0$ are the initial spatial velocity and material angular velocity, respectively; $\bar{\boldsymbol{\eta}}_c$ and $\bar{\boldsymbol{\vartheta}}_c$ are the prescribed displacement and rotation vectors at the beam ends where Dirichlet Boundary Conditions (BCs) are enforced, whereas $\bar{\boldsymbol{n}}_c$ and $\bar{\boldsymbol{m}}_c$ are the prescribed concentrated force and couple associated with the Neumann BCs.

3.2. Neumann boundary conditions

While Dirichlet BCs can straightforwardly be enforced in the RKMK framework, the collocated Neumann BCs must be expressed in terms of the primary unknowns of the problem, namely $\dot{\boldsymbol{v}}$, and $\dot{\boldsymbol{\omega}}$. To overcome this issue, several alternatives have been proposed. Marino et al. [47] exploited the SO(3)-consistent Newmark time-integrator to express the Neumann BCs in terms of the primary unknowns. Although it was an elegant solution, the method relied on the specific choice of the time integrator whose accuracy is limited to the second-order. Unfortunately, this limitation affects also higher-order time integrators as in the RKMK case. De Lorenzis et al. [64] developed an enhanced collocation (EC) treatment consisting in enforcing both balance and Neumann conditions at the boundary. In the geometrically exact beam framework, the EC Neumann BCs becomes

$$\mu\dot{\boldsymbol{v}} = \mathbf{R}\widetilde{\boldsymbol{K}}\mathbb{C}_N\boldsymbol{\Gamma}_N + \mathbf{R}\mathbb{C}_N\boldsymbol{\Gamma}_{N,s} + \bar{\boldsymbol{n}} + \frac{C^*}{l_s}\left[\bar{\boldsymbol{n}}_c - \mathbf{R}\mathbb{C}_N\boldsymbol{\Gamma}_N\right], \tag{22}$$

[1] With the symbol $\sim$ we mark elements of so(3), that is the set of 3×3 skew-symmetric matrices. In this context, they are used to represent curvature matrices and infinitesimal incremental rotations. Furthermore, we recall that for any skew-symmetric matrix $\widetilde{\boldsymbol{a}} \in \mathrm{so}(3)$, $\boldsymbol{a} = \mathrm{axial}(\widetilde{\boldsymbol{a}})$ indicates the axial vector of $\widetilde{\boldsymbol{a}}$ such that $\widetilde{\boldsymbol{a}}\boldsymbol{h} = \boldsymbol{a} \times \boldsymbol{h}$, for any $\boldsymbol{h} \in \mathbb{R}^3$, where $\times$ is the cross product.

$$\boldsymbol{j}\dot{\boldsymbol{\omega}} + \widetilde{\boldsymbol{\omega}}\boldsymbol{j}\boldsymbol{\omega} = \mathbf{R}\widetilde{\boldsymbol{K}}\mathbb{C}_M\boldsymbol{K}_M + \mathbf{R}\mathbb{C}_M\boldsymbol{K}_{M,s} + \widetilde{\boldsymbol{c}}_{,s}\mathbf{R}\mathbb{C}_N\boldsymbol{\Gamma}_N + \bar{\boldsymbol{m}} + \frac{C^*}{l_s}\left[\bar{\boldsymbol{m}}_c - \mathbf{R}\mathbb{C}_M\boldsymbol{K}_M\right], \tag{23}$$

where C^* is a suitable constant, while l_s is a characteristic length, taken as half the distance between the first two collocation points encountered starting from the Neumann boundary. As suggested in [64], this constant is set $C^* = 4$.

3.3. Time-discretized version of the governing equations in the first-order form

To apply the RKMK to the above second-order governing equations, Eqs. (16) (17), the problem must be transformed into a first order differential problem in time. This is possible through Eqs. (8) and (12) leading to the following complete set of first order (in time) differential equations

$$\begin{cases} \dot{\boldsymbol{\eta}} = \boldsymbol{v}\,, \\ \mu\dot{\boldsymbol{v}} = \boldsymbol{\psi}_v\,, \\ \dot{\boldsymbol{\vartheta}} = d\exp^{-1}_{\widetilde{\boldsymbol{\vartheta}}}(\boldsymbol{\omega})\,, \\ \boldsymbol{j}\dot{\boldsymbol{\omega}} = \chi_\omega\,, \end{cases} \tag{24}$$

where we have set

$$\boldsymbol{\psi}_v = \mathbf{R}\widetilde{\boldsymbol{K}}\mathbb{C}_N\boldsymbol{\Gamma}_N + \mathbf{R}\mathbb{C}_N\boldsymbol{\Gamma}_{N,s} + \bar{\boldsymbol{n}}, \tag{25}$$

$$\chi_\omega = -\widetilde{\boldsymbol{\omega}}\boldsymbol{j}\boldsymbol{\omega} + \widetilde{\boldsymbol{K}}\mathbb{C}_M\boldsymbol{K}_M + \mathbb{C}_M\boldsymbol{K}_{M,s} + \mathbf{R}^{\mathsf{T}}\boldsymbol{c}_{,s} \times \mathbb{C}_N\boldsymbol{\Gamma}_N + \mathbf{R}^{\mathsf{T}}\bar{\boldsymbol{m}}. \tag{26}$$

Concerning $s = \{0, L\}$, in the case of Neumann BCs, the system is modified as follows

$$\begin{cases} \dot{\boldsymbol{\eta}} = \boldsymbol{v}\,, \\ \mu\dot{\boldsymbol{v}} = \boldsymbol{\psi}_v + \frac{C^*}{l_s}\left[\bar{\boldsymbol{n}}_c - \mathbf{R}\mathbb{C}_N\boldsymbol{\Gamma}_N\right], \\ \dot{\boldsymbol{\vartheta}} = d\exp^{-1}_{\widetilde{\boldsymbol{\vartheta}}}(\boldsymbol{\omega})\,, \\ \boldsymbol{j}\dot{\boldsymbol{\omega}} = \chi_\omega + \frac{C^*}{l_s}\left[\bar{\boldsymbol{m}}_c - \mathbf{R}\mathbb{C}_M\boldsymbol{K}_M\right]. \end{cases} \tag{27}$$

While time integration of the first and third equations in Eqs. (24) or (27) has been extensively discussed above (see Section 2.3), to compute the velocities at time t^{n+1}

$$\boldsymbol{v}^{n+1} = \boldsymbol{v}^n + \sum_{r=1}^{N} b_r \boldsymbol{k}_{\boldsymbol{v}_r}\,, \tag{28}$$

$$\boldsymbol{\omega}^{n+1} = \boldsymbol{\omega}^n + \sum_{r=1}^{N} b_r \boldsymbol{k}_{\boldsymbol{\omega}_r} \tag{29}$$

we must deploy the RK scheme to the second and fourth equations in Eqs. (24) or (27) to compute the following incremental quantities

$$\boldsymbol{k}_{\boldsymbol{v}_r} = \boldsymbol{\psi}^n_{v_r}/\mu\,, \tag{30}$$

$$\boldsymbol{k}_{\boldsymbol{\omega}_r} = \boldsymbol{j}^{n-1}_r \chi^n_{\omega_r}\,, \tag{31}$$

where the right-hand sides depend on the configuration and angular velocity at time $t^n_r = t^n + c_r h$

$$\boldsymbol{\psi}^n_{v_r} = \boldsymbol{\psi}^n_{v_r}\left(\boldsymbol{c}^n_r, \mathbf{R}^n_r, \bar{\boldsymbol{n}}^n_r\right), \qquad \chi^n_{\omega_r} = \chi^n_{\omega_r}\left(\boldsymbol{c}^n_r, \mathbf{R}^n_r, \boldsymbol{\omega}^n_r, \bar{\boldsymbol{m}}^n_r\right), \tag{32}$$

where $\boldsymbol{c}^n_r = \boldsymbol{c}^n + \boldsymbol{\eta}^n_r$, $\mathbf{R}^n_r = \exp(\widetilde{\boldsymbol{\vartheta}}^n_r)\mathbf{R}^n$, with

$$\boldsymbol{\eta}^n_r = \sum_{l=1}^{N} d_{rl}\boldsymbol{k}_{\boldsymbol{\eta}_l} \tag{33}$$

$$\boldsymbol{\vartheta}^n_r = \sum_{l=1}^{N} d_{rl}\boldsymbol{k}_{\boldsymbol{\vartheta}_l}, \tag{34}$$

and

$$\boldsymbol{v}^n_r = \boldsymbol{v}^n + \sum_{l=1}^{N} d_{rl}\boldsymbol{k}_{\boldsymbol{v}_l}\,, \tag{35}$$

$$\boldsymbol{\omega}^n_r = \boldsymbol{\omega}^n + \sum_{l=1}^{N} d_{rl}\boldsymbol{k}_{\boldsymbol{\omega}_l}\,. \tag{36}$$

Note that also the external loads must be computed at time t^n_r as $\bar{\boldsymbol{n}}^n_r = \bar{\boldsymbol{n}}(t^n + c_r h)$ and $\bar{\boldsymbol{m}}^n_r = \bar{\boldsymbol{m}}(t^n + c_r h)$.

3.4. Space discretization of the time-discretized governing equations

At each stage r, we essentially need to compute $\boldsymbol{k}_{\eta_r}$, $\boldsymbol{k}_{v_r}$, $\boldsymbol{k}_{\vartheta_r}$ and $\boldsymbol{k}_{\omega_r}$ that depend also on the spatial variable s. We introduce the isogeometric space discretization as follows

$$\boldsymbol{k}_{\eta_r}(u) \simeq \sum_{j=0}^{\mathrm{n}} R_{j,p}(u)\check{\boldsymbol{k}}_{\eta_r j}\,, \qquad \boldsymbol{k}_{v_r}(u) \simeq \sum_{j=0}^{\mathrm{n}} R_{j,p}(u)\check{\boldsymbol{k}}_{v_r j}\,, \tag{37}$$

$$\boldsymbol{k}_{\vartheta_r}(u) \simeq \sum_{j=0}^{\mathrm{n}} R_{j,p}(u)\check{\boldsymbol{k}}_{\vartheta_r j}\,, \qquad \boldsymbol{k}_{\omega_r}(u) \simeq \sum_{j=0}^{\mathrm{n}} R_{j,p}(u)\check{\boldsymbol{k}}_{\omega_r j}\,, \tag{38}$$

where $(\check{\circ})_j$ denotes the jth control value of the related field, while $R_{j,p}$ is the jth NURBS basis function of degree p depending on the parametric abscissa $u \in [0,\,1]$.

Following the IGA-C framework, Eqs. (24) or (27) are discretized using Eqs. (37) and (38) and then collocated at the Greville points [52]. The space-discretized version of the governing equations at the rth stage, with $r = 1, 2, \dots, N$, read as

$$\begin{cases} \boldsymbol{M}_c\check{\boldsymbol{k}}_{\eta_r} & = \boldsymbol{v}^n_{r\,c}\,, \\ \boldsymbol{M}_c\check{\boldsymbol{k}}_{v_r} & = \dfrac{\boldsymbol{\psi}^n_{v_r c}}{\mu}\,, \\ \boldsymbol{M}_c\check{\boldsymbol{k}}_{\vartheta_r} & = d\exp^{-1}_{\tilde{\boldsymbol{\vartheta}}^n_{r\,c}}(\boldsymbol{\omega}^n_{r\,c})\,, \\ \boldsymbol{M}_c\check{\boldsymbol{k}}_{\omega_r} & = \boldsymbol{j}^{-1}{}^n_{r\,c}\boldsymbol{\chi}^n_{\omega_r c}\,, \end{cases} \tag{39}$$

where $(\circ)_c$ denotes quantities evaluated at the collocation points $\boldsymbol{u}_c = [u_0,\,u_1,\,\dots,\,u_{\mathrm{n}}]^{\mathsf{T}}$. $\boldsymbol{M}_c$ is the $3(\mathrm{n}+1)\times 3(\mathrm{n}+1)$ plain basis functions matrix

$$\boldsymbol{M}_c = \begin{bmatrix} \boldsymbol{R}(u_0)_{0,p} & \boldsymbol{R}(u_0)_{1,p} & \cdots & \boldsymbol{R}(u_0)_{\mathrm{n},p} \\ \boldsymbol{R}(u_1)_{0,p} & \boldsymbol{R}(u_1)_{1,p} & \cdots & \boldsymbol{R}(u_1)_{\mathrm{n},p} \\ \vdots & \vdots & \ddots & \vdots \\ \boldsymbol{R}(u_{\mathrm{n}-1})_{0,p} & \boldsymbol{R}(u_{\mathrm{n}-1})_{1,p} & \cdots & \boldsymbol{R}(u_{\mathrm{n}-1})_{\mathrm{n},p} \\ \boldsymbol{R}(u_{\mathrm{n}})_{0,p} & \boldsymbol{R}(u_{\mathrm{n}})_{1,p} & \cdots & \boldsymbol{R}(u_{\mathrm{n}})_{\mathrm{n},p} \end{bmatrix}, \tag{40}$$

where $\boldsymbol{R}(u_i)_{j,p} = R(u_i)_{j,p}\mathbf{id}$, being $\mathbf{id}$ the 3×3 identity matrix.

Importantly, we remark that: *i*) the matrix $\boldsymbol{M}_c$ is the same for all unknowns and depends only on the space discretization of the problem, meaning that no update of $\boldsymbol{M}_c$ is required; *ii*) Eq. (39) are uncoupled, meaning that from one linear system of $12(\mathrm{n}+1)\times 12(\mathrm{n}+1)$ equations, one can reduce the problem to 4 linear systems of size $3(\mathrm{n}+1)\times 3(\mathrm{n}+1)$; *iii*) BCs, either Neumann or Dirichlet, do not alter the structure of the mass matrix $\boldsymbol{M}_c$.

The above three features are crucial to determine the extraordinary efficiency of the method. There is no need to solve any linear system as $\boldsymbol{M}_c$ can be inverted once for all offline. The formulation does not require any linearization of the rotational balance equations due to the nonlinear term associated with the angular velocity [47,48]. It is also noted that no special treatments, like mass lumping or predictor multi-corrector schemes, are needed to bypass matrix inversion. Mass scaling techniques are neither necessary. Moreover, since the equations are decoupled, there is an appealing potentiality in terms of parallelization.

3.5. Consistent update of the governing equations in the RKMK stages

Making use of Eqs. (37) to (38), we can rewrite Eqs. (35) and (36) in terms of control variables

$$\boldsymbol{\eta}^n_r(u) = \sum_{j=0}^{\mathrm{n}} R_{j,p}(u)\check{\boldsymbol{\eta}}_{rj}\,, \tag{41}$$

$$\boldsymbol{\vartheta}^n_r(u) = \sum_{j=0}^{\mathrm{n}} R_{j,p}(u)\check{\boldsymbol{\vartheta}}^n_{rj}\,, \tag{42}$$

$$\boldsymbol{v}^n_r(u) = \sum_{j=0}^{\mathrm{n}} R_{j,p}(u)\check{\boldsymbol{v}}^n_{rj}\,, \tag{43}$$

$$\boldsymbol{\omega}^n_r(u) = \sum_{j=0}^{\mathrm{n}} R_{j,p}(u)\check{\boldsymbol{\omega}}^n_{rj}\,, \tag{44}$$

where we have set

$$\check{\boldsymbol{\eta}}_{rj} = \sum_{l=1}^{N} d_{rl}\check{\boldsymbol{k}}_{\eta_l}\,, \tag{45}$$

$$\check{\boldsymbol{\vartheta}}^n_{rj} = \sum_{l=1}^{N} d_{rl}\check{\boldsymbol{k}}_{\vartheta_l}\,, \tag{46}$$

$$\check{\boldsymbol{v}}^n_{rj} = \check{\boldsymbol{v}}^n_j + \sum_{l=1}^{N} d_{rl}\check{\boldsymbol{k}}_{\boldsymbol{v}_{lj}} \,, \tag{47}$$

$$\check{\boldsymbol{\omega}}^n_{rj} = \check{\boldsymbol{\omega}}^n_j + \sum_{l=1}^{N} d_{rl}\check{\boldsymbol{k}}_{\boldsymbol{\omega}_l} \,. \tag{48}$$

Moreover, at time t_r the geometry is updated as follows

$$\boldsymbol{c}^n_r(u) = \sum_{j=0}^{\mathrm{n}} R_{j,p}(u)\left(\check{\boldsymbol{c}}^n_j + \check{\boldsymbol{\eta}}_{rj}\right), \tag{49}$$

$$\mathbf{R}^n_r(u) = \exp(\widetilde{\boldsymbol{\vartheta}}^n_r(u))\mathbf{R}^n(u)\,. \tag{50}$$

The consistent update of the rotational matrix allows to update some configuration-related quantities, such as the spatial inertia tensor

$$\boldsymbol{j}^n_r(u) = \mathbf{R}^n_r(u)\boldsymbol{J}(u){\mathbf{R}^{\mathsf{T}}}^n_r(u)\,, \tag{51}$$

and the material curvature tensor, $\widetilde{\boldsymbol{K}}$, along with its space derivative, $\widetilde{\boldsymbol{K}},_s$

$$\widetilde{\boldsymbol{K}}^n_r = \widetilde{\boldsymbol{K}}^n + {\mathbf{R}^{\mathsf{T}}}^n d\exp_{\widetilde{\boldsymbol{\vartheta}}^n_r}(\widetilde{\boldsymbol{\vartheta}}^n_r,_s)\mathbf{R}^n \tag{52}$$

$$\begin{aligned}\widetilde{\boldsymbol{K}}^n_r,_s = {} & \widetilde{\boldsymbol{K}},^n_s - \widetilde{\boldsymbol{K}}^n {\mathbf{R}^{\mathsf{T}}}^n d\exp_{\widetilde{\boldsymbol{\vartheta}}^n_r}(\widetilde{\boldsymbol{\vartheta}}^n_r,_s)\mathbf{R}^n + {\mathbf{R}^{\mathsf{T}}}^n d\exp_{\widetilde{\boldsymbol{\vartheta}}^n_r}(\widetilde{\boldsymbol{\vartheta}}^n_r,_s)\mathbf{R}^n\widetilde{\boldsymbol{K}}^n + \\ & + {\mathbf{R}^{\mathsf{T}}}^n\left(d\exp_{\widetilde{\boldsymbol{\vartheta}}^n_r}(\widetilde{\boldsymbol{\vartheta}}^n_r,_s)\right),_s \mathbf{R}^n\,.\end{aligned} \tag{53}$$

Using the closed-form expressions for $d\exp_{\widetilde{\boldsymbol{\vartheta}}}(\circ)$ (see Appendix B) allows to efficiently compute the right hand sides of the governing equations, $\boldsymbol{\psi}^n_{v_r}$ and $\chi^n_{\omega_r}$, at each stage r of the RKMK scheme.

3.6. Consistent time-stepping geometry update

A similar approach allows to update consistently the configuration manifold at time t^{n+1}. Once that the Nth stage of the RK scheme has been completed, the solutions of the stages are linearly combined using the weights b_r. Control variables are updated as

$$\check{\boldsymbol{c}}^{n+1} = \check{\boldsymbol{c}}^n + \sum_{r=1}^{N} b_r\check{\boldsymbol{k}}_{\boldsymbol{\eta}_r}\,, \qquad \check{\boldsymbol{\vartheta}}^{n+1} = \sum_{r=1}^{N} b_r\check{\boldsymbol{k}}_{\boldsymbol{\vartheta}_r}\,, \tag{54}$$

$$\check{\boldsymbol{v}}^{n+1} = \check{\boldsymbol{v}}^n + \sum_{r=1}^{N} b_r\check{\boldsymbol{k}}_{\boldsymbol{v}_r}\,, \qquad \check{\boldsymbol{\omega}}^{n+1} = \check{\boldsymbol{\omega}}^n + \sum_{r=1}^{N} b_r\check{\boldsymbol{k}}_{\boldsymbol{\omega}_r}\,, \tag{55}$$

while the rotation operator, together with curvature variables and beam strain measures, at t^{n+1} are consistently updated at the collocation points as done in [47] .

4. Numerical applications

In this section, the proposed method is tested through a series of numerical applications. First, we assess the ability of the method to achieve high-order accuracy both in time and space. This is done considering two challenging benchmark tests: a swinging flexible pendulum and a cantilever beam under transversal tip load. These tests have already been adopted to asses the accuracy and efficiency of the formulations proposed in past works (see e.g., [47,48,58,59]) where Time accuracy was limited to the second-order. Then, two demanding tests on initially curved beams are proposed.

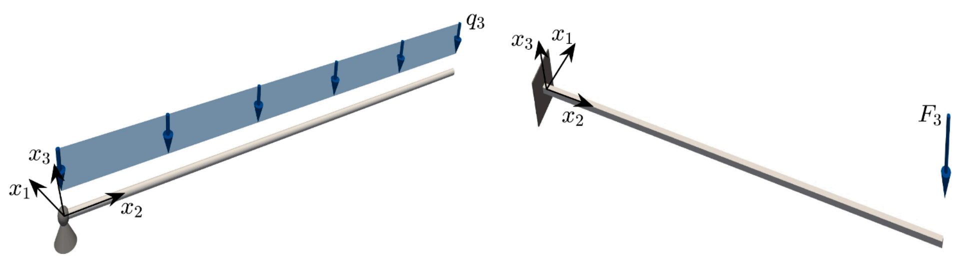

(a) Swinging flexible pendulum, $q_3 = -0.8475\,\mathrm{N/m}$. (b) Cantilever beam under tip load, $F_3 = -100\,\mathrm{N}$.

Fig. 1. Initial configurations and load conditions of the two benchmark tests.

Table 1
Material properties of the two benchmark tests.

	$A\,[\mathrm{m}^2]$	$E\,[\mathrm{N/m}^2]$	$\nu\,[-]$	$\rho\,[\mathrm{kg/m}^3]$
Swinging pendulum	$7.854e-5$	$5.00e6$	0.5	$1.1E3$
Cantilever beam	$1.000e-4$	$2.10e11$	0.2	$7.8E3$

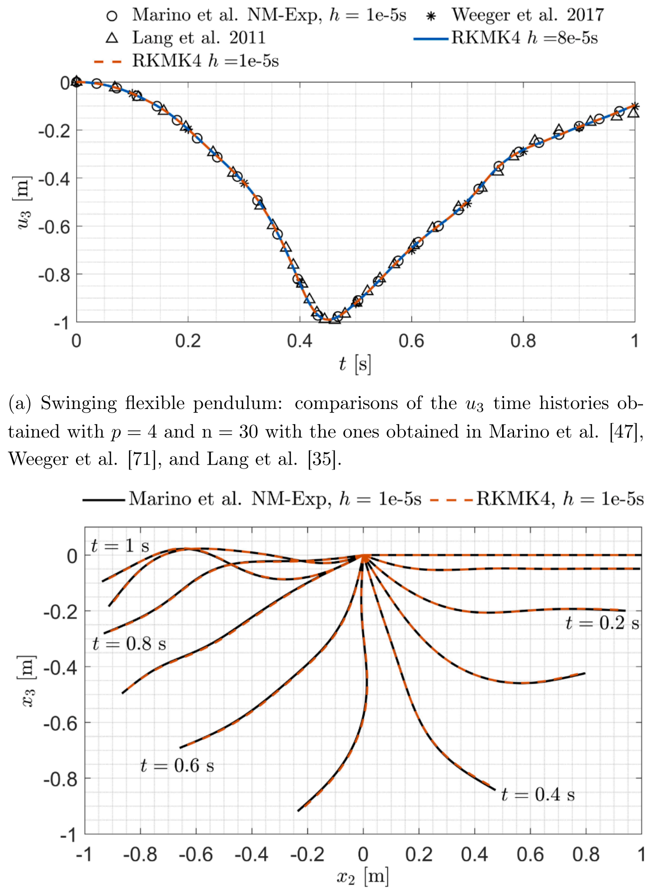

(a) Swinging flexible pendulum: comparisons of the u_3 time histories obtained with $p = 4$ and n = 30 with the ones obtained in Marino et al. [47], Weeger et al. [71], and Lang et al. [35].

(b) Swinging flexible pendulum: comparison of the deformed shapes at significant time instants with the ones obtained in Marino et al. [47].

Fig. 2. Swinging flexible pendulum: comparisons of the tip vertical displacement, u_3, time histories and deformed shapes configurations; results for the present formulation are obtained with RKMK4 and variable step size.

4.1. Time and space accuracy assessment

Fig. 1 shows the initial shape and load conditions of a swinging flexible pendulum in a gravitational field, $q_3 = -0.8475$ N/m (Fig. 1(a)), and a cantilever beam under tip load, $F_3 = 100$ N (Fig. 1(b)).

Both structures have a length $L = 1$ m. The first features a circular cross-section of diameter $d = 0.01$ m, while the second has a square cross-section of side $t = 0.01$ m. Both beams are made of linear elastic materials, whose properties are reported in Table 1.

Figs. 2 and 3 show comparisons of the results obtained using a fourth-order accurate RKMK scheme (RKMK4) with the ones taken from the literature adopting both explicit [35,47] and implicit [35,42,58] time integrators. An excellent agreement is observed for both cases, even with larger time step sizes compared to the literature ones.

To assess the high-order accuracy in time and space we compute the L_2-norm of the error over a grid of fixed points as $err_{L_2} = ||\boldsymbol{u}^r - \boldsymbol{u}^h||/||\boldsymbol{u}^r||$, where $\boldsymbol{u}^h$ is the approximated displacement, while $\boldsymbol{u}^r$ is the reference solution. In order to assess the impact of

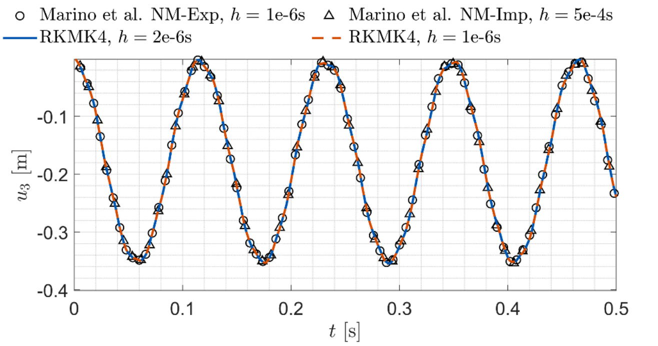

(a) Cantilever beam under tip load: u_3 time histories obtained with $p = 4$ and $\mathrm{n} = 20$ with the ones obtained by Marino et al. adopting explicit (black circular markers) (indicated with NM-Exp) [47] and implicit (black triangular markers) [58] Newmark time integrators.

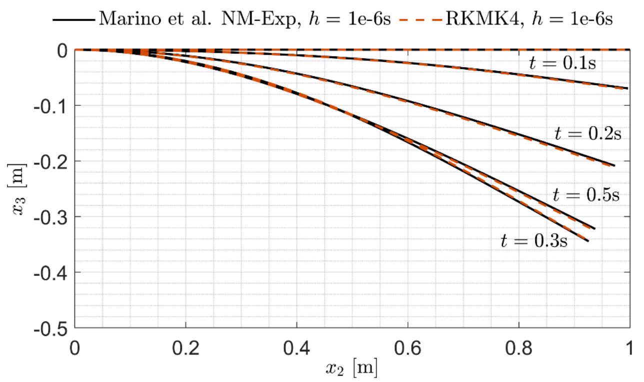

(b) Cantilever beam under tip load: comparison of the deformed shapes at significant time instants with the ones obtained in Marino et al. [47] using a Newmark explicit time integrator (indicated with NM-Exp).

Fig. 3. Comparisons of the tip vertical displacement, u_3, time histories and deformed shapes configurations for the two benchmark tests with the ones in [47]; results for the present formulation are obtained with RKMK4 and different step sizes.

higher-order methods on the computational efficiency, we also compute the total CPU time T_{CPU} of the same simulations carried out for the time-convergence analysis. This permits evaluating the error, err_{L_2}, as a function of both time step size h and CPU time, T_{CPU}.

4.1.1. High-order accuracy for the swinging flexible pendulum

Concerning the time accuracy, we fix the space discretization to $p = 4$ and $\mathrm{n} = 30$, while for the space accuracy we adopt a sixth-order accurate RKMK (RKMK6) scheme with a time step of $h = 5 \times 10^{-6}$ s. For the time convergence, $\boldsymbol{u}^r$ is computed using RKMK6 and $h = 1 \times 10^{-6}$ s, while for the space convergence we use $p = 8$ and $\mathrm{n} = 100$. Fig. 4(a) shows the convergence rates in time obtained with second-, third-, fourth-, and sixth-order RKMK schemes (indicated with RKMK2, RKMK3, RKMK4, and RKMK6, respectively). An excellent agreement with the expected rates is observed. In Fig. 4, we also plot err_{L_2} vs the computational time T_{CPU}. It can be seen that higher-order schemes (RKMK4 and RKMK6) permit achieving, with lower T_{CPU}, solutions that are order of magnitude more accurate than the ones obtained with RKMK2 and RKMK3. Also, note that the accuracy of the RKMK2 is limited compared to the other methods even when using very small h (see the red curves in Fig. 4(a)-(b)).

Space convergence rates are plotted in Fig. 4(c) for $p = 2, 4, 6, 8$ versus the number n of collocation points. Also in this case, an excellent agreement with the expected rates is observed, especially for $p = 4$ and $p = 6$. The slower rate for $p = 8$ might be ascribed to a residual time error which limits higher accuracy in space.

4.1.2. High-order accuracy for the cantilever beam

In this case, the reference solutions are computed using RKMK6 and $h = 1 \times 10^{-8}$ s for the time accuracy, and using $p = 8$ and $\mathrm{n} = 100$ for the space accuracy. Fig. 5(a) shows the time convergence rates for various RKMK schemes. In this case, the space discretization is fixed to $p = 4$ and $\mathrm{n} = 30$. Excellent rates are achieved for all the time-discretization schemes adopted. Also for this test, we analyse

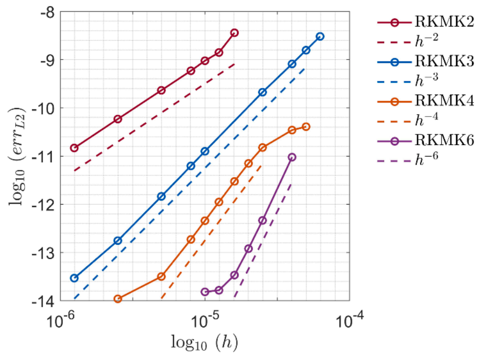

(a) Time convergence at time $t = 0.02$ s: L_2-norm of the error err_{L_2} vs time step size h.

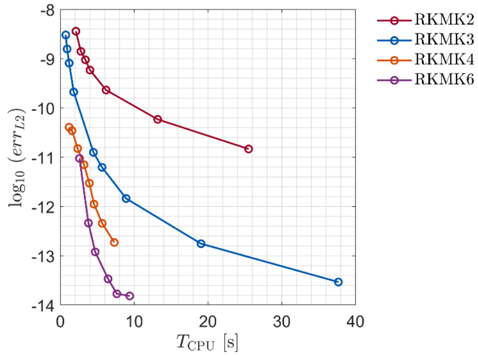

(b) Time convergence at time $t = 0.02$ s: L_2-norm of the error err_{L_2} vs computational time T_{CPU}.

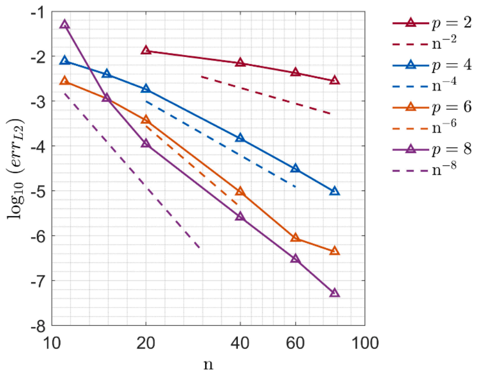

(c) Space convergence at time $t = 0.1$ s.

Fig. 4. Time and space convergence plots for the swinging flexible pendulum.

Table 2
Exact initial geometry of the circular arch with $p = 2$ NURBS basis functions and 3 control points.

	x_1 [m]	x_2 [m]	x_3 [m]	w [−]
$\check{\boldsymbol{P}}_1$	0	0	0	1
$\check{\boldsymbol{P}}_2$	0	$\sqrt{3}/\pi$	0	$\sqrt{3}/2$
$\check{\boldsymbol{P}}_3$	$3/2\pi$	$3\sqrt{3}/2\pi$	0	1

the efficiency of different RKMK schemes in Fig. 5(b). Similar to the pendulum case (see Fig. 4(b)), higher order methods exhibit a significant reduction in terms of computational time as larger h allows to achieve numerical solutions that are as accurate as the ones obtained with RKMK2 and RKMK3 schemes. We also remark that the computational times for the cantilever beam case are higher compared to the ones for the pendulum case (Fig. 4(b)) as smaller time steps are employed for this test.

Space convergence rates are plotted in Fig. 5(c) for $p = 2, 4, 6, 8$, versus the number of collocation points, n. In this study, a RKMK6 scheme with $h = 1 \times 10^{-7} s$ is used. Similarly to the previous case, good convergences are achieved, especially for $p = 4$ and $p = 6$.

4.2. Flexural vibrations of a circular arch

In this test, we investigate a 60°–circular arch of radius $R = 3/\pi$ m. The arch is placed in the (x_1, x_2) plane and it features a total length of 1 m. It is clamped at $[0, 0, 0]^{\mathrm{T}}$, and it is loaded by a concentrated couple M_3 at the free end (see Fig. 6). The exact geometry is reconstructed with NURBS of degree $p = 2$ and 3 control points, see Table 2 for their coordinates and weights.

The same material and cross-section adopted for the cantilever beam are employed here. The couple M_3 is applied instantaneously with an intensity of $\pi E J_1/3$ Nm such that, in the static regime, the beam would deform into a straight cantilever. The load is kept constant for 0.25 s, and then removed. Through k-refinement, that provides C^{p-1} inter-element continuity [72], the centroid line is discretized with NURBS basis functions with $p = 4$ and $\mathrm{n} = 30$. The simulation time is set to 1 s, with a time step size of $h = 1 \times 10^{-6}$ s. Snapshots of the deformed beam at some selected time instants are plotted in Fig. 7(a). The time history of the x_1 and x_2 components

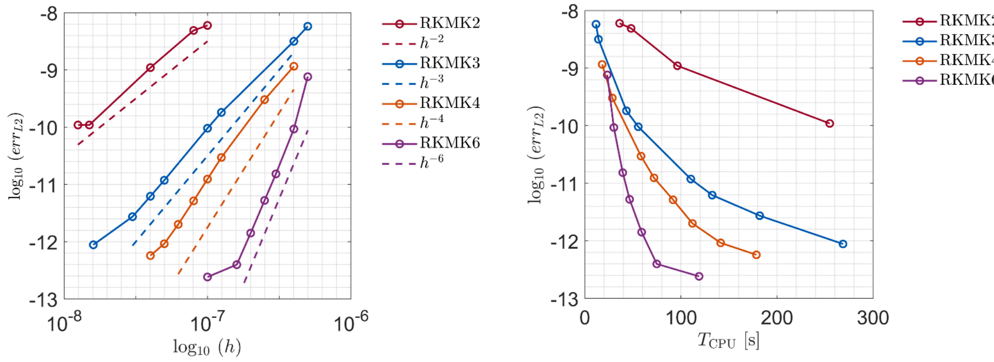

(a) Time convergence at time $t = 0.0024\,\mathrm{s}$: L_2-norm of the error err_{L_2} vs time step size h.

(b) Time convergence at time $t = 0.0024\,\mathrm{s}$: L_2-norm of the error err_{L_2} vs computational time T_{CPU}.

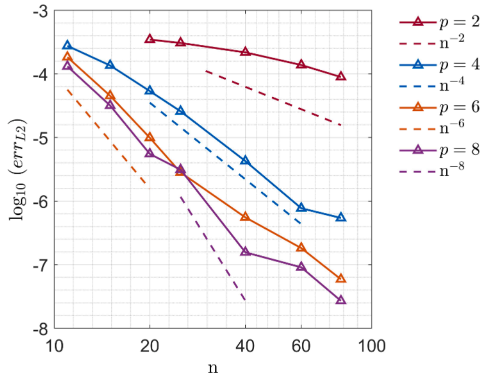

(c) Space convergence at time $t = 0.001\,\mathrm{s}$.

Fig. 5. Time and space convergence plots for the cantilever beam.

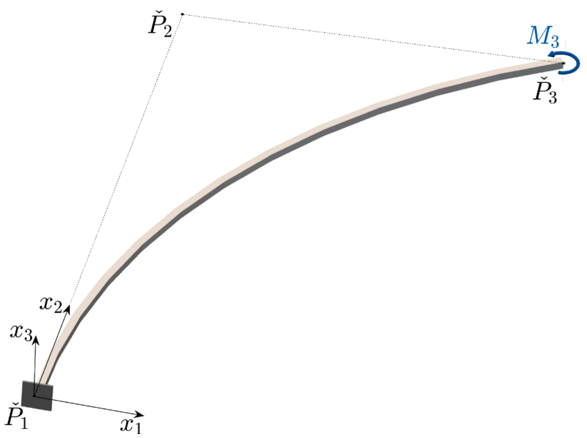

Fig. 6. Circular arch initial geometry.

of the tip position, $\check{\boldsymbol{P}}_3$, are shown in Fig. 7(b). Under the action of the concentrated couple ($t < 0.25\,\mathrm{s}$), the beam start oscillating around the straight position, with an amplitude in the x_1-direction of approximately $3/2\pi$ (see the blue solid line in Fig. 7(b)). As the load is removed ($t > 0.25\,\mathrm{s}$), the beam keeps vibrating around its initial position. Higher vibration modes are observed in the x_2-direction (see the orange solid line in Fig. 7(c)). The behavior of the vibrating arch is well depicted also in Fig. 7(c), where it is shown x_3 component of the curvature, $K_{\check{\boldsymbol{P}}_3}(3)$. The horizontal red solid line corresponds to the initial curvature, $K_{0\check{\boldsymbol{P}}_3}(3)$.

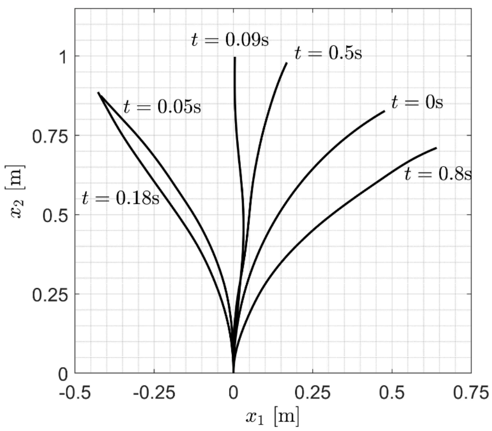

(a) Deformed configurations, plane (x_1, x_2) view.

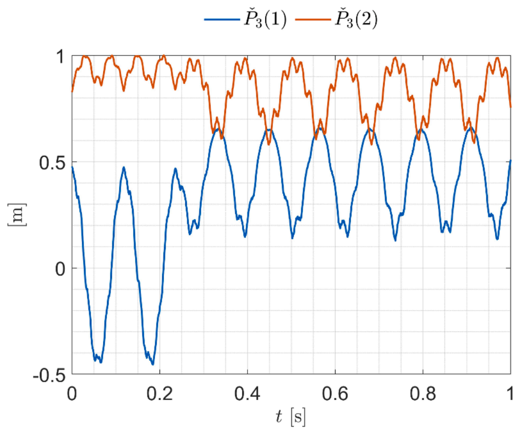

(b) Time history of the tip position along x_1, and x_2.

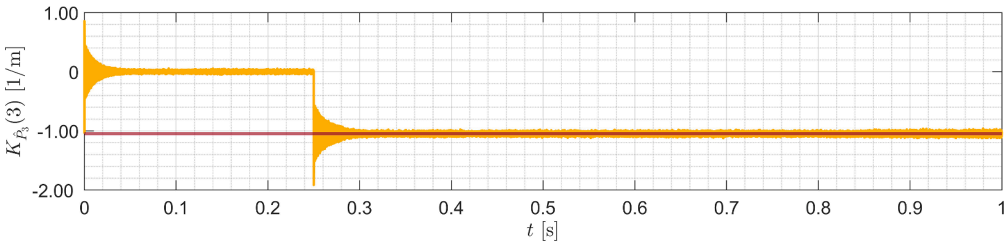

(c) Time history of the material curvature component (yellow solid line) along x_3, $K_{\hat{P}_3}(3)$; note that the red straight line refers to the initial curvature component $K_{0\hat{P}_3}(3)$.

Fig. 7. Circular arch vibrations: deformation snapshots, time histories of tip position and material curvature components.

(a) Initial configuration.

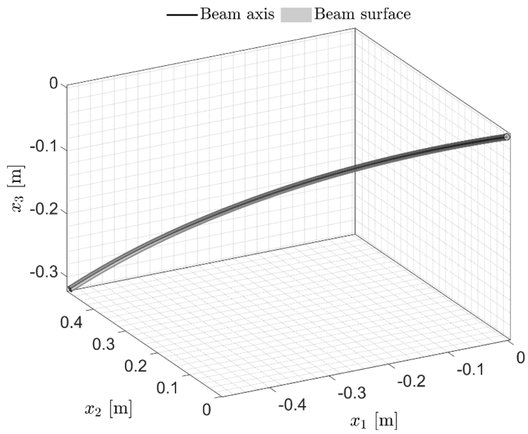

(b) 3D view of the initial geometry.

Fig. 8. Spinning curved beam: initial configuration and geometry.

4.3. Spinning of a curved beam

Finally, we present the case of a curved beam that spins in a gravitational field (Fig. 8) . The first end of the beam, located at the origin of the reference frame, (x_1, x_2, x_3), is hinged. The initial beam centroid is defined by the curve $\boldsymbol{c}_0(s) = [R(\cos(s) - 1),\ R\sin(s),\ -s/\pi]^{\mathrm{T}}$, with $s \in [0,\ \pi/2]$ and $R = 3/(2\pi)$, representing a quarter of an helix coil. We prescribe an initial angular velocity of $\omega_3^0 = 2\pi$ rad/s directed along x_3. The beam is also subjected to its self-weight, $q_3 = -0.8475$ N/m. The beam has a circular cross-section with diameter $d = 0.01$ m. The material properties are the same as for the swinging pendulum case.

Deformed shapes, displacement and velocity time histories are plotted in Figs. 9 and 10, respectively. The beam undergoes large displacements, with complex 3D rotations involving a combination of rigid and flexible motions. Different combinations of degree p

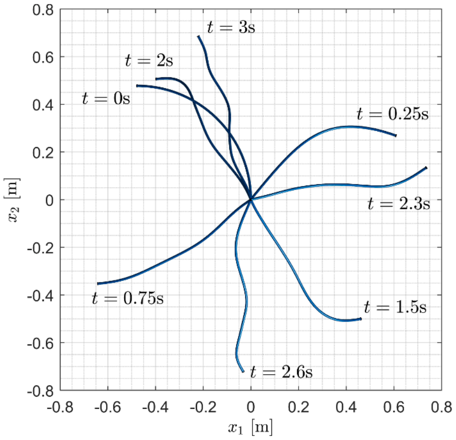

(a) Plane (x_1, x_2) view.

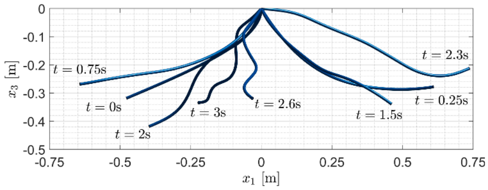

(b) Plane (x_1, x_3) view.

Fig. 9. Spinning curved beam: deformed shapes obtained with $p = 6$, n = 61 and $h = 1e - 4s$.

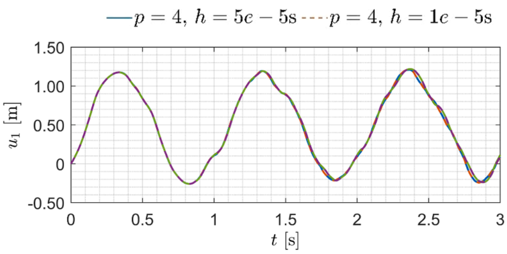

(a) Displacement component along x_1.

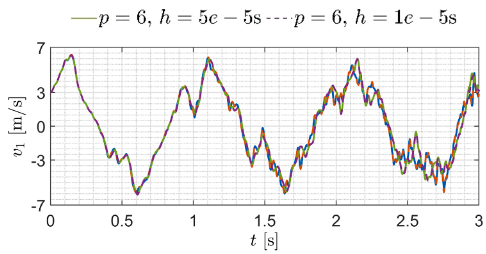

(b) Velocity component along x_1.

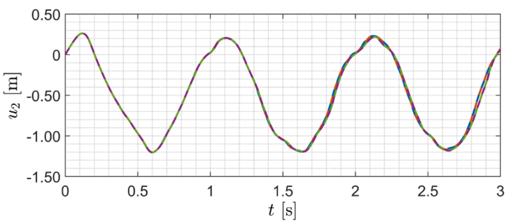

(c) Displacement component along x_2.

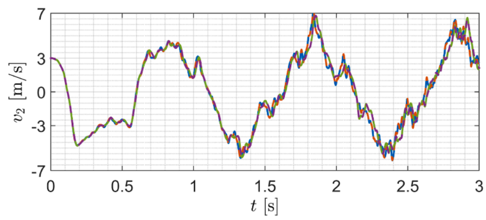

(d) Velocity component along x_2.

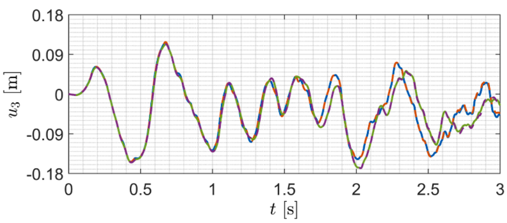

(e) Displacement component along x_3.

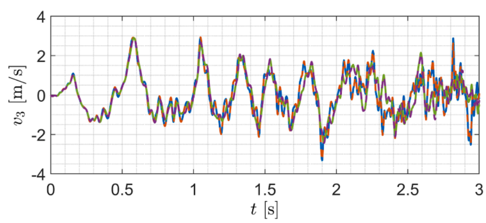

(f) Velocity component along x_3.

Fig. 10. Spinning curved beam: tip displacement and velocity time histories obtained with n = 81.

and time step size h are reported. Importantly, it is noticed that the space error is dominant, especially in u_3 (see Fig. 10(e)). Indeed, the case $p = 6$, $h = 5 \times 10^{-5}$ s is basically the same as the case $p = 6$, $h = 1 \times 10^{-5}$ s. This demonstrate that, having an high-order accurate solver in time, the IGA atribute of k-refinement can fully be exploited without being limited by the time accuracy.

5. Conclusion

In this paper, we presented an isogeometric collocation (IGA-C) formulation for the dynamics of geometrically exact shear-deformable beams, featuring high-order accuracy in time and space. The Runge-Kutta-Munthe-Kaas (RKMK) method, namely a manifold-consistent reformulation of the classical Runge-Kutta (RK) method, is taken beyond the rigid body boundaries and, apparently for the first time, it has been extended to the problem of geometrically exact beams. Basically, within each stage of the classical RK scheme, the consistent system of equation is solved on the tangent space of the configuration manifold $\mathbb{R}^3 \times SO(3)$ for incremental displacements, rotations, and translational and angular velocities. This leads to a formulation that does not require any linearization of the rotational balance equations due to the nonlinear term associated with the angular velocity. Furthermore, adopting the "enhanced collocation" treatment for the Neumann boundary conditions permits obtaining uncoupled Boundary Conditions (BCs) leading to an explicit setting that naturally circumvents matrix inversion. Through a series of benchmark tests, we demonstrate that accuracy up to sixth-order in time can be achieved fully exploiting the high-order space-accuracy typical of IGA-C. Applications to curved beam problems further indicates the potentialities of the proposed framework in simulating the dynamics of systems with complex geometries. We believe that the proposed method posses great potentialities for any rotational dynamic problem, in particular we plan to extend the formulation to the explicit dynamics of geometrically exact shells, possibly with non linear materials, and to shape changing, programmable systems.

CRediT authorship contribution statement

Giulio Ferri: Writing – review & editing, Writing – original draft, Methodology, Investigation, Formal analysis, Conceptualization; **Enzo Marino:** Writing – review & editing, Writing – original draft, Supervision, Methodology, Investigation, Funding acquisition, Formal analysis, Conceptualization.

Data availability

Data will be made available on request.

Declaration of competing interest

The authors declare that they have no known competing financial interests or personal relationships that could have appeared to influence the work reported in this paper.

Acknowledgments

EM was partially supported by the European Union - Next Generation EU, in the context of The National Recovery and Resilience Plan, Investment 1.5 Ecosystems of Innovation, Project Tuscany Health Ecosystem (THE). (CUP: B83C22003920001).

EM was also partially supported by the National Centre for HPC, Big Data and Quantum Computing funded by the European Union within the Next Generation EU recovery plan. (CUP B83C22002830001).

EM and GF were partially supported by the UniFI project IGA4Stent - "Patient-tailored stents: an innovative computational isogeoemtric analysis approach for 4D printed shape changing devices". (CUP B55F21007810001).

EM and GF were also partially supported by the PRIN 2022 project NonlinEar Phenomena in floaTing offshore wind tUrbiNEs (NEPTUNE), prot. 2022W7SKTL. (CUP B53D23006480006), funded by the Italian MUR.

These supports are gratefully acknowledged.

Appendix A.

For convenience, we report from Table A.1 to Table A.4 a list of *Butcher tableaux* suitable for second-, third-, fourth- and sixth-order explicit RK methods. As it can be seen, to achieve sixth-order accuracy in time, seven stages ($N = 7$) are required, meaning that the linear system must be solved seven times to compute the unknown quantities at time t^{n+1}.

Table A.1
Butcher tableau for second-order RK methods (RK2).

0	0	0
1/2	1/2	0
	0	1

Table A.2
Butcher tableau for third-order RK methods (RK3).

0	0	0	0
1/2	1/2	0	0
1	-1	1/2	0
	1/6	2/3	1/6

Table A.3
Butcher tableau for fourth-order RK methods (RK4).

0	0	0	0	0
1/2	1/2	0	0	0
1/2	0	1/2	0	0
1	0	0	1	0
	1/6	1/3	1/3	1/6

Table A.4
Butcher tableau for fourth-order RK methods (RK6).

0	0	0	0	0	0	0	0
1/3	1/3	0	0	0	0	0	0
2/3	0	2/3	0	0	0	0	0
1/3	1/12	1/3	-1/12	0	0	0	0
1/2	-1/16	9/8	-3/16	-3/8	0	0	0
1/2	9/8	-3/8	-3/4	1/2	0	0	0
1	9/44	-9/11	63/44	18/11	0	-16/11	0
	11/120	0	27/40	27/40	-4/15	-4/15	11/120

Appendix B.

In this appendix we first provide the proof of Eq. (12) and then we give the analytical expression of the derivative of the exponential map of SO(3), as well as the its inverse, $d\exp^{-1}_{\widetilde{\boldsymbol{\vartheta}}}(\circ)$, which is crucial for our formulation.

Proof of Eq. (12)

For small $t \geq 0$, we have

$$\mathbf{R}(t,s) = \exp(\widetilde{\boldsymbol{\vartheta}}(t,s))\mathbf{R}_0(s)\,. \tag{56}$$

Omitting the variable s for brevity, the time derivative of the above equation is given by

$$\dot{\mathbf{R}}(t) = d\exp_{\widetilde{\boldsymbol{\vartheta}}}\dot{\widetilde{\boldsymbol{\vartheta}}}(t)\exp(\widetilde{\boldsymbol{\vartheta}}(t))\mathbf{R}_0\,, \tag{57}$$

with

$$d\exp_{\widetilde{\boldsymbol{\vartheta}}} = \frac{\exp(\mathrm{ad}_{\widetilde{\boldsymbol{\vartheta}}}) - \mathbf{id}_{\mathrm{SO}(3)}}{\mathrm{ad}_{\widetilde{\boldsymbol{\vartheta}}}}\,, \tag{58}$$

where $\mathrm{ad}_{\widetilde{\boldsymbol{\vartheta}}}$ denotes the adjoint operator $\widetilde{\boldsymbol{\vartheta}} \mapsto \mathrm{ad}_{\widetilde{\boldsymbol{\vartheta}}} := [\widetilde{\boldsymbol{\vartheta}}, \circ\,]$ and $[\,\circ, \circ\,]$ indicates the Lie brackets (see e.g., [73,74]). $\mathbf{id}_{\mathrm{SO}(3)}$ is the identity of SO(3).

Equating (11) and (57) and making use of (56) we obtain the sought result given in Eq. (12).

Derivatives of the exponential map

We start by recalling the definition of exponential map for SO(3)

$$\exp(\widetilde{\boldsymbol{\vartheta}}) = \mathbf{id}_{\mathrm{SO}(3)} + \frac{\sin(\vartheta)}{\vartheta}\,\widetilde{\boldsymbol{\vartheta}} + \frac{1-\cos(\vartheta)}{\vartheta^2}\,\widetilde{\boldsymbol{\vartheta}}^2\,, \tag{59}$$

where $\widetilde{\boldsymbol{\vartheta}} \in \mathrm{so}(3)$ and $\vartheta = ||\boldsymbol{\vartheta}||$.

For any $\boldsymbol{a} \in \mathbb{R}^3$, we have the following definitions

$$d\exp_{\widetilde{\boldsymbol{\vartheta}}}(\boldsymbol{a}) = \boldsymbol{a} - \frac{1-\cos(\vartheta)}{\vartheta^2}\,\widetilde{\boldsymbol{\vartheta}}\boldsymbol{a} + \frac{(1-\sin(\vartheta))/\vartheta}{\vartheta^2}\,\widetilde{\boldsymbol{\vartheta}}\big(\widetilde{\boldsymbol{\vartheta}}\boldsymbol{a}\big)\,, \tag{60}$$

$$d\exp^{-1}_{\widetilde{\boldsymbol{\vartheta}}}(\boldsymbol{a}) = \boldsymbol{a} + \frac{1}{2}\,\widetilde{\boldsymbol{\vartheta}}\boldsymbol{a} + \frac{\vartheta\cot(\vartheta/2) - 2}{2\vartheta^2}\,\widetilde{\boldsymbol{\vartheta}}\big(\widetilde{\boldsymbol{\vartheta}}\boldsymbol{a}\big)\,. \tag{61}$$

In the above sections of the paper we have set $d\exp_{\tilde{\vartheta}}(\widetilde{\boldsymbol{a}}) = \mathrm{skw}\left[d\exp_{\tilde{\vartheta}}(\boldsymbol{a})\right] \in \mathrm{so}(3)$ and $d\exp_{\tilde{\vartheta}}^{-1}(\widetilde{\boldsymbol{a}}) = \mathrm{skw}\left[d\exp_{\tilde{\vartheta}}^{-1}(\boldsymbol{a})\right] \in \mathrm{so}(3)$. For the sake of completeness, we also report the series expansions of the above equations, obtained approximating the exponential map of SO(3),

$$d\exp_{\tilde{\vartheta}} \simeq \sum_{i=0}^{\infty} \frac{(-1)^i}{(1+i)!} (\mathrm{ad}_{\tilde{\vartheta}})^i \,, \qquad d\exp_{\tilde{\vartheta}}^{-1} \simeq \sum_{i=0}^{\infty} \frac{(-1)^i B_i}{(1+i)!} (\mathrm{ad}_{\tilde{\vartheta}})^i \,, \tag{62}$$

where B_i is the ith Bernoulli number, while $\mathrm{ad}\ \tilde{\mathrm{o}}$ is the adjoint operator of the Lie algebra, so(3) [60]. Bypassing such time-consuming series expansions significantly improves the efficiency of the formulation compared to [47,48].

References

[1] Y. Yang, H. Zheng, M.V. Sivaselvan, A rigorous and unified mass lumping scheme for higher-order elements, Comput. Methods Appl. Mech. Eng. 319 (2017) 491–514. https://doi.org/10.1016/j.cma.2017.03.011

[2] H. Gravenkamp, C. Song, J. Zhang, On mass lumping and explicit dynamics in the scaled boundary finite element method, Comput. Methods Appl. Mech. Eng. 370 (2020) 113274. https://doi.org/10.1016/j.cma.2020.113274

[3] S. Held, S. Eisenträger, W. Dornisch, An efficient mass lumping scheme for isogeometric analysis based on approximate dual basis functions, Technische Mechanik 44 (2024) 14–46. https://doi.org/10.24352/UB.OVGU-2024-052

[4] Y. Voet, E. Sande, A. Buffa, A mathematical theory for mass lumping and its generalization with applications to isogeometric analysis, Comput. Methods Appl. Mech. Eng. 410 (2023) 116033. 2212.03614. https://doi.org/10.1016/j.cma.2023.116033

[5] C. Anitescu, C. Nguyen, T. Rabczuk, X. Zhuang, Isogeometric analysis for explicit elastodynamics using a dual-basis diagonal mass formulation, Comput. Methods Appl. Mech. Eng. 346 (2019) 574–591. https://doi.org/10.1016/j.cma.2018.12.002

[6] X. Li, D. Wang, On the significance of basis interpolation for accurate lumped mass isogeometric formulation, Comput. Methods Appl. Mech. Eng. 400 (2022) 115533. https://doi.org/10.1016/j.cma.2022.115533

[7] T.-H. Nguyen, R.R. Hiemstra, S. Eisenträger, D. Schillinger, Towards higher-order accurate mass lumping in explicit isogeometric analysis for structural dynamics, Comput. Methods Appl. Mech. Eng. 417 (2023) 116233. A Special Issue in Honor of the Lifetime Achievements of T. J. R. Hughes, https://doi.org/10.1016/j.cma.2023.116233

[8] S. Duczek, H. Gravenkamp, Mass lumping techniques in the spectral element method: on the equivalence of the row-sum, nodal quadrature, and diagonal scaling methods, Comput. Methods Appl. Mech. Eng. 353 (2019) 516–569. https://doi.org/10.1016/j.cma.2019.05.016

[9] A. Tkachuk, M. Bischoff, Direct and sparse construction of consistent inverse mass matrices: general variational formulation and application to selective mass scaling, Int. J. Numer. Meth. Eng. (October) (2015) 1102–1119. https://doi.org/10.1002/nme

[10] A.K. Schaeuble, A. Tkachuk, M. Bischoff, Variationally consistent inertia templates for B-spline- and NURBS-based FEM: inertia scaling and customization, Comput. Methods Appl. Mech. Eng. 326 (2017) 596–621. https://doi.org/10.1016/j.cma.2017.08.035

[11] B. Oesterle, A. Tkachuk, M. Bischoff, Finite element technology-based selective mass scaling for shear deformable structural element formulations, in: COMPDYN Proceedings, National Technical University of Athens, 2023. https://doi.org/10.7712/120123.10534.20662

[12] L.M. Krauß, R. Thierer, M. Bischoff, B. Oesterle, Intrinsically selective mass scaling with hierarchic plate formulations, Comput. Methods Appl. Mech. Eng. 432 (2024). https://doi.org/10.1016/j.cma.2024.117430

[13] J.C. Butcher, A history of Runge-Kutta methods, Appl. Numer. Math. 20 (3) (1996) 247–260. https://doi.org/10.1016/0168-9274(95)00108-5

[14] J.H.E. Cartwright, O. Piro, The dynamics of Runge-Kutta methods, Int. J. Bifurcation Chaos 02 (03) (1992) 427–449. https://doi.org/10.1142/S0218127492000641

[15] J.C. Simo, A finite strain beam formulation. The three-dimensional dynamic problem. Part I, Comput. Methods Appl. Mech. Eng. 49 (1) (1985) 55–70.

[16] L. Simo, J. C. and Vu-Quoc, A three-dimensional finite-strain rod model. Part II: computational aspects, Comput. Methods Appl. Mech. Eng. 58 (1) (1986) 79–116.

[17] L. Simo, J. C. and Vu-Quoc, On the dynamics in space of rods undergoing large motions - a geometrically exact approach, Comput. Methods Appl. Mech. Eng. 66 (2) (1988) 125–161.

[18] J.C. Simo, K.K. Wong, Unconditionally stable algorithms for rigid body dynamics that exactly preserve energy and momentum, Int. J. Numer. Methods Eng. 31 (1) (1991) 19–52.

[19] J.C. Simo, D.D. Fox, M.S. Rifai, S. Univeristy, On a stress resultant geometrically exact shell model. Part III computational aspects …- Simo, J. C. and fox, D. D. and Rifai, M. S. - CMAME - (1990).pdf, Comput. Methods Appl. Mech. Eng. 79 (1990) 21–70.

[20] J.C. Simo, M.S. Rifai, D.D. Fox, On a stress resultant geometrically exact shell model. Part VI: conserving algorithms for non-linear dynamics, Int. J. Numer. Methods Eng. 34 (1992) 117–164. https://doi.org/10.1002/nme.1620340108

[21] Y. Choquet-Bruhat, C. Dewitt-Morette, Analysis, Manifolds and Physics Part I: Basics, Elsevier B.V., 1996.

[22] H. Munthe-Kaas, Runge-Kutta methods on Lie groups, BIT Numer. Math. 38 (1) (1998) 92–111. https://doi.org/10.1007/BF02510919

[23] H. Munthe-Kaas, High order Runge-Kutta methods on manifolds, Appl. Numer. Math. 29 (1) (1999) 115–127. https://doi.org/10.1016/S0168-9274(98)00030-0

[24] E. Celledoni, A. Marthinsen, B. Owren, Commutator-Free Lie Group Methods, Technical Report, 2003.

[25] E. Celledoni, E. Çokaj, A. Leone, D. Murari, B. Owren, Lie group integrators for mechanical systems, Int. J. Comput. Math. 99 (2022) 58–88. https://doi.org/10.1080/00207160.2021.1966772

[26] T. Lee, Geometric control of quadrotor UAVs transporting a cable-suspended rigid body, IEEE Trans. Control Syst. Technol. 26 (2018) 255–264. https://doi.org/10.1109/TCST.2017.2656060

[27] A. Cardona, M. Geradin, A beam finite element non-linear theory with finite rotations, Int. J. Numer. Methods Eng. 26 (September 1987) (1988) 2403–2438.

[28] A. Ibrahimbegović, M.A.L. Mikdad, Finite rotations in dynamics of beams and implicit time-stepping schemes, Int. J. Numer. Methods Eng.41 (November 1996) (1998) 781–814.

[29] G. Jelenic, M.a. Crisfield, Interpolation of rotational variables in nonlinear dynamics of 3D beams, Int. J. Numer. Methods Eng. 1222 (February 1997) (1998) 1193–1222.

[30] G. Jelenić, M.A. Crisfield, Geometrically exact 3D beam theory: implementation of a strain-invariant finite element for statics and dynamics, Comput. Methods Appl. Mech. Eng. 171 (1–2) (1999) 141–171.

[31] J. Mäkinen, Critical study of newmark-scheme on manifold of finite rotations, Comput. Methods Appl. Mech. Eng. 191 (2001) 817–828.

[32] I. Romero, F. Armero, An objective finite element approximation of the kinematics of geometrically exact rods and its use in the formulation of an energy-momentum conserving scheme in dynamics, Int. J. Numer. Methods Eng. 54 (12) (2002) 1683–1716.

[33] J. Mäkinen, Total Lagrangian Reissner's geometrically exact beam element without singularities, Int. J. Numer. Methods Eng. 70 (October 2006) (2007) 1009–1048.

[34] J. Mäkinen, Rotation manifold SO(3) and its tangential vectors, Comput. Mech. 42 (6) (2008) 907–919.

[35] H. Lang, J. Linn, M. Arnold, Multi-body dynamics simulation of geometrically exact Cosserat rods, Multibody Syst. Dyn. 25 (3) (2011) 285–312.

[36] O. Brüls, A. Cardona, M. Arnold, Lie group generalized-α time integration of constrained flexible multibody systems, Mech. Mach. Theory 48 (2012) 121–137.

[37] E. Zupan, M. Saje, D. Zupan, Quaternion-based dynamics of geometrically nonlinear spatial beams using the Runge-Kutta method, Finite Elem. Anal. Des. 54 (2012) 48–60.

[38] E. Zupan, M. Saje, D. Zupan, Dynamics of spatial beams in quaternion description based on the Newmark integration scheme, Comput. Mech. 51 (1) (2013) 47–64.

[39] V. Sonneville, A. Cardona, O. Brüls, Geometrically exact beam finite element formulated on the special Euclidean group SE(3), Comput. Methods Appl. Mech. Eng. 268 (3) (2014) 451–474.
[40] T.-N. Le, J.-M. Battini, M. Hjiaj, A consistent 3D corotational beam element for nonlinear dynamic analysis of flexible structures, Comput. Methods Appl. Mech. Eng. 269 (2014) 538–565.
[41] P.M. Almonacid, Explicit symplectic momentum-conserving time-stepping scheme for the dynamics of geometrically exact rods, Finite Elem. Anal. Des. 96 (2015) 11–22.
[42] O. Weeger, B. Narayanan, M.L. Dunn, Isogeometric collocation for nonlinear dynamic analysis of Cosserat rods with frictional contact, Nonlinear Dyn. 91 (2017) 1–15.
[43] A. Cammarata, L. Greco, D. Castello, M. Cuomo, An implicit time integrator for Cosserat rods based on the spherical Bézier interpolation, Comput. Methods Appl. Mech. Eng. 445 (2025). https://doi.org/10.1016/j.cma.2025.118195
[44] S. Eugster, Geometric Continuum Mechanics and Induced Beam Theories, 75, Springer, 2015.
[45] C. Meier, A. Popp, W.A. Wall, Geometrically exact finite element formulations for slender beams: Kirchhoff-Love theory versus simo-reissner theory, Arch. Comput. Methods Eng. (2017). https://doi.org/10.1007/s11831-017-9232-5
[46] P. Krysl, L. Endres, Explicit Newmark/Verlet algorithm for time integration of the rotational dynamics of rigid bodies, Int. J. Numer. Methods Eng. 62 (15) (2005) 2154–2177.
[47] E. Marino, J. Kiendl, L. De Lorenzis, Explicit isogeometric collocation for the dynamics of three-dimensional beams undergoing finite motions, Comput. Methods Appl. Mech. Eng. 343 (2019) 530–549. https://doi.org/10.1016/j.cma.2018.09.005
[48] G. Ferri, J. Kiendl, A. Reali, E. Marino, A fully explicit isogeometric collocation formulation for the dynamics of geometrically exact beams, Comput. Methods Appl. Mech. Eng. 431 (2024) 117283. https://doi.org/10.1016/j.cma.2024.117283
[49] T.J.R. Hughes, J.A. Cottrell, Y. Bazilevs, Isogeometric analysis: CAD, finite elements, NURBS, exact geometry and mesh refinement, Comput. Methods Appl. Mech. Eng. 194 (39–41) (2005) 4135–4195.
[50] J.a. Cottrell, A. Reali, Y. Bazilevs, T.J.R. Hughes, et al., Isogeometric analysis of structural vibrations, Comput. Methods Appl. Mech. Eng. 195 (41–43) (2006) 5257–5296.
[51] J.A. Cottrell, T.J.R. Hughes, Y. Bazilevs, Isogeometric Analysis: Toward Integration of CAD and FEA, JohnWiley & Sons, Ltd Registered, 2009.
[52] F. Auricchio, L.B. Da Veiga, T.J.R. Hughes, a. Reali, G. Sangalli, et al., Isogeometric collocation methods, Math. Models Methods Appl. Sci. 20 (11) (2010) 2075–2107.
[53] F. Auricchio, F. Calabrò, T.J.R. Hughes, A. Reali, G. Sangalli, et al., A simple algorithm for obtaining nearly optimal quadrature rules for NURBS-based isogeometric analysis, Comput. Methods Appl. Mech. Eng. 249–252 (2012) 15–27.
[54] F. Fahrendorf, S. Shivanand, B.V. Rosic, M.S. Sarfaraz, T. Wu, L. De Lorenzis, H.G. Matthies, Collocation Methods and Beyond in Non-linear Mechanics, Springer International Publishing, 2022, pp. 449–504. https://doi.org/10.1007/978-3-030-92672-4_16
[55] F. Auricchio, L. Beirão da Veiga, T.J.R. Hughes, a. Reali, G. Sangalli, et al., Isogeometric collocation for elastostatics and explicit dynamics, Comput. Methods Appl. Mech. Eng. 249–252 (2012) 2–14.
[56] J.A. Evans, R.R. Hiemstra, T.J.R. Hughes, A. Reali, et al., Explicit higher-order accurate isogeometric collocation methods for structural dynamics, Comput. Methods Appl. Mech. Eng. (2018) 491–514. https://doi.org/10.1016/j.cma.2018.04.008
[57] D. Schillinger, J. Evans, A. Reali, M. Scott, T.J.R. Hughes, et al., Isogeometric collocation: cost comparison with Galerkin methods and extension to adaptive hierarchical NURBS discretizations, Comput. Methods Appl. Mech. Eng. 267 (2013) 170–232.
[58] E. Marino, J. Kiendl, L. De Lorenzis, Isogeometric collocation for implicit dynamics of three-dimensional beams undergoing finite motions, Comput. Methods Appl. Mech. Eng. 356 (2019) 548–570. https://doi.org/10.1016/J.CMA.2019.07.013
[59] G. Ferri, E. Marino, An isogeometric analysis formulation for the dynamics of geometrically exact viscoelastic beams and beam systems with arbitrarily curved initial geometry, Comput. Methods Appl. Mech. Eng. 431 (2024) 117261. https://doi.org/10.1016/j.cma.2024.117261
[60] E. Marino, Isogeometric collocation for three-dimensional geometrically exact shear-deformable beams, Comput. Methods Appl. Mech. Eng. 307 (2016) 383–410.
[61] E. Marino, Locking-free isogeometric collocation formulation for three-dimensional geometrically exact shear-deformable beams with arbitrary initial curvature, Comput. Methods Appl. Mech. Eng. 324 (2017) 546–572.
[62] O. Weeger, D. Schillinger, R. Müller, Mixed isogeometric collocation for geometrically exact 3D beams with elasto-visco-plastic material behavior and softening effects, Comput. Methods Appl. Mech. Eng. 399 (2022) 115456. https://doi.org/10.1016/j.cma.2022.115456
[63] G. Ferri, D. Ignesti, E. Marino, An efficient displacement-based isogeometric formulation for geometrically exact viscoelastic beams, Comput. Methods Appl. Mech. Eng. 417 (2023) 116413. 2307.10106. https://doi.org/10.1016/j.cma.2023.116413
[64] L. De Lorenzis, J.A. Evans, T.J.R. Hughes, A. Reali, et al., Isogeometric collocation: neumann boundary conditions and contact, Comput. Methods Appl. Mech. Eng. 284 (2015) 21–54.
[65] O. Weeger, B. Narayanan, L. De Lorenzis, J. Kiendl, M.L. Dunn, et al., An isogeometric collocation method for frictionless contact of Cosserat rods, Comput. Methods Appl. Mech. Eng. 321 (2017) 361–382.
[66] H. Gomez, A. Reali, G. Sangalli, Accurate, efficient, and (iso)geometrically flexible collocation methods for phase-field models, J. Comput. Phys. 262 (2014) 153–171.
[67] D. Schillinger, M.J. Borden, H.K. Stolarski, Isogeometric collocation for phase-field fracture models, Comput. Methods Appl. Mech. Eng. 284 (2015) 583–610. https://doi.org/10.1016/J.CMA.2014.09.032
[68] M. Torre, S. Morganti, A. Nitti, M.D. de Tullio, F.S. Pasqualini, A. Reali, Isogeometric mixed collocation of nearly-incompressible electromechanics in finite deformations for cardiac muscle simulations, Comput. Methods Appl. Mech. Eng. 411 (2023) 116055. https://doi.org/10.1016/J.CMA.2023.116055
[69] J.C. Butcher, On Runge-Kutta processes of high order, J. Aust. Math. Soc. 4 (2) (1964) 179 – 194. Cited by: 252; All Open Access, Bronze Open Access, . https://doi.org/10.1017/S1446788700023387
[70] E. Reissner, On one-dimensional finite-strain beam theory: the plane problem, Zeitschrift für angewandte Mathematik und Mechanik angewandte Mathematik und Physik ZAMP 23 (1972) 795–804.
[71] O. Weeger, S.-K. Yeung, M.L. Dunn, Isogeometric collocation methods for Cosserat rods and rod structures, Comput. Methods Appl. Mech. Eng. 316 (2017) 100–122.
[72] J.a. Cottrell, T.J.R. Hughes, a. Reali, Studies of refinement and continuity in isogeometric structural analysis, Comput. Methods Appl. Mech. Eng. 196 (41–44) (2007) 4160–4183.
[73] W. Rossmann, Lie Groups an Introduction Through Linear Groups, Oxford University Press, oxford gra edition, 2002.
[74] A. Iserles, H.Z. Munthe-kaas, S.P. Nørsett, A. Zanna, Lie-group methods, Acta Numer. (2000) 215–365.